Article

Applied Spectroscopy
www.s-a-s.org

Applied Spectroscopy
2017, Vol. 71(12) 2595–2607

DOI: 10.1177/0003702817715042
journals.sagepub.com/home/asp
SAGE

Label-Free Raman Hyperspectral Imaging of Single Cells Cultured on Polymer Substrates

Faris Sinjab[1], Giovanna Sicilia[2], Dustin W. Shipp[1], Maria Marlow[2], and Ioan Notingher[1]

Abstract

While Raman hyperspectral imaging has been widely used for label-free mapping of biomolecules in cells, these measurements require the cells to be cultured on weakly Raman scattering substrates. However, many applications in biological sciences and engineering require the cells to be cultured on polymer substrates that often generate large Raman scattering signals. Here, we discuss the theoretical limits of the signal-to-noise ratio in the Raman spectra of cells in the presence of polymer signals and how optical aberrations may affect these measurements. We show that Raman spectra of cells cultured on polymer substrates can be obtained using automatic subtraction of the polymer signals and demonstrate the capabilities of these methods in two important applications: tissue engineering and in vitro toxicology screening of drugs. Apart from their scientific and technological importance, these applications are examples of the two most common measurement configurations: (1) cells cultured on an optically thick polymer substrate measured using an immersion/dipping objective; and (2) cells cultured on a transparent polymer substrate and measured using an inverted optical microscope. In these examples, we show that Raman hyperspectral data sets with sufficient quality can be successfully acquired to map the distribution of common biomolecules in cells, such as nucleic acids, proteins, and lipids, as well as detecting the early stages of apoptosis. We also discuss strategies for further improvements that could expand the application of Raman hyperspectral imaging on polymer substrates even further in biomedical sciences and engineering.

Keywords

Raman spectroscopy, hyperspectral imaging, cells, polymer substrates, background correction

Revised: 15 March 2017; Accepted: 10 May 2017

Introduction

Spontaneous Raman microspectroscopy (RMS) is a powerful noninvasive and label-free technique for cell biology,[1,2] offering specific chemical imaging of biomolecule distribution and quantification at the single-cell level[3–7] monitoring of biological processes such as apoptosis,[8–11] stem cell differentiation,[12–14] effects of drugs on cancer cells,[15–17] and host–pathogen interactions.[18] Raman microspectroscopy measurements of biological systems requires the detection of low numbers of inelastically scattered photons, and in order to measure these weak signals, low-background substrates such as fused quartz, MgF_2, or CaF_2 are often chosen to minimize undesirable background photons.[19,20] Using such substrates, RMS allows Raman spectra to be obtained from single cells with diffraction limited spatial resolution. When combined with sample raster scanning (a full Raman spectrum is collected at each pixel), this allows Raman hyperspectral imaging to be carried out, which provides rich three-dimensional (3D) data sets (two spatial dimensions and one spectral dimension).

Nevertheless, cells in nature are rarely isolated and exist in a variety of complex microenvironments, such as the extracellular matrix in tissues. For real applications in biological sciences and engineering, quartz, MgF_2, or CaF_2 are rarely used. Many research areas involve studying cells in the presence of other materials that are important for

[1]School of Physics and Astronomy, University of Nottingham, Nottingham, UK
[2]School of Pharmacy, University of Nottingham, Nottingham, UK

Corresponding authors:
Faris Sinjab, University of Nottingham, University Park, University of Nottingham, Nottingham, Nottinghamshire NG7 2RD, UK.
Email: faris.sinjab@nottingham.ac.uk
Ioan Notingher
Email: ioan.notingher@nottingham.ac.uk

the particular application being investigated. Polymers are widely used in biomedical engineering applications (e.g., tissue engineering scaffolds), and due to their low cost and availability, polymer containers are used for routine cell culture or cell biology assays. A popular biocompatible and biodegradable polymer is PLGA (poly(D,L-lactide-*co*-glycolide)), which is commonly used as a scaffold in tissue engineering applications[21] and has also been proposed as a biomedical material for selective adhesion of tumor cells by specific nanopatterning of thin PLGA films.[22] Another example is polystyrene (PS), which is ubiquitous in the form of cell culture plates in bioscience laboratories. Polystyrene is desirable as it is inexpensive, safely disposable, and can be used for high-throughput measurement, which is important in applications such as anti-cancer drug screening.

Such polymer substrates are usually compatible with most other optical microscopy techniques such as fluorescence and phase contrast. However, they produce a large background Raman spectrum as the polymers themselves typically have both a larger Raman scattering cross-section compared to the cells. This comparatively large Raman scattering signal from the polymer introduces an associated shot noise, which can easily envelope the Raman scattering from the cells. For this reason, measurements on such substrates are usually avoided with RMS. However, it would clearly be advantageous if RMS was compatible with such systems, as it has the potential to offer additional vibrational spectroscopic insight into cell–cell or cell–substrate interactions on these polymer materials, as well as expanding its use to a range of applications where routine plastic ware is used (well-plates, Petri dishes, culture flasks, etc.).

Here, based on a simple geometric optics model, we discuss the theoretical signal-to-noise (S/N) limits of performing RMS of cells cultured on polymer substrates and how optical aberrations may influence results. We then demonstrate Raman hyperspectral imaging of cells in two different systems, where several post-processing steps, which are already available in the literature, are applied to the data. The first example involves Raman imaging of ovarian cancer cells on thin PLGA substrates with nanotextured topography, measured through a quartz coverslip. The second involves measuring breast cancer cells treated with an anti-cancer drug directly through standard PS culture wells, where aberrations will be significant, resulting in a large background signal.

Materials and Methods

Raman Microspectroscopy

The instrument used for studying ovarian cells (OVCAR3) cultured on PLGA substrates is based on the instrument described in Sinjab et al.,[23] but using only a single excitation beam on the optical axis. A 785 nm CW Ti:sapphire laser is used for excitation (SpectraPhysics), attenuated to 100–200 mW (measured at sample). The beam is delivered through a modified inverted microscope (Olympus IX71), with a motorized scanning stage (Proscan III, Prior scientific). An *f*/1.8 imaging spectrometer (LS 785, Princeton Instruments) with a 128×1024 charge-coupled device (CCD; iDus 401 BR-DD, Andor) was used for the measurement of the Raman scattered light. OVCAR3 cells adhered to PLGA films (0.4–0.6 mm thick) were placed onto a fused quartz substrate ($t = 0.18$ mm, SPS supplies) and measured using a 60×, 1.2 NA water immersion objective with a working distance of 0.28 mm (UPLANsapo, Olympus, Japan).

The instrument used for measuring the breast cancer cells (MCF-7) in PS well-pates had a 785 nm continuous wave laser (I0785SM0300PA-MOPA, Innovative Photonics Solutions) with 50 mW of total power delivered to the sample. The beam was directed through an inverted microscope (Eclipse Ti-S, Nikon, Japan) with a motorized stage (Proscan II, Prior Scientific), with Raman backscattered light collected by a spectrometer (Model 2500+ High Performance Raman Module, RiverD, Netherlands) equipped with a 128×1024 CCD (iDus 401 BR-DD, Andor). Home-built LabVIEW software (National Instruments) was used for raster scanning measurements. MCF-7 cells on standard disposable PS culture wells (thickness $t = 1.0$ mm, Corning 35 mm TC-Treated Culture Dishes, product number 430165), using a 50×, 1.2 NA, oil-immersion objective, optimized for RMS, with a working distance of 1.5 mm (RiverD, The Netherlands).

Cell Cultures

Human breast adenocarcinoma cell line (MCF-7; American Type Culture Collection) and human ovarian carcinoma cell line (Ovcar3; U.S. National Cancer Institute) were grown in standard T75 flasks. MCF-7 cells were grown in RPMI 1640 media supplemented with 10% fetal bovine serum and L-glutamine. Ovcar3 cells were grown in RPMI 1640 media supplemented with 10% fetal bovine serum, L-glutamine, and 0.01 mg/mL bovine insulin. Both cell lines were maintained at 37 °C in a 5% CO_2 humidified environment.

Ovcar3 Cells Cultured on PLGA Films

Ovcar3 cells were seeded on PLGA films at a density of 6×105 cells/film and incubated at 37 °C for 2 h. Afterwards, cells were fixed in 4% paraformaldehyde at room temperature for 10 min and stored in PBS before being transferred under the Raman microscope.

Paclitaxel Preparation

Paclitaxel (LC Laboratories) was initially dissolved in DMSO to get a solution of 0.01 M and subsequently diluted

with MCF-7 growth medium to afford stock solutions with a drug concentration in the range of 0.1–50 μM. The concentration of DMSO reached 0.5% (w/v) in the 50 μM Paclitaxel solution and had no significant influence ($P > 0.05$) on cell viability compared to the untreated cells. In all the remaining working solutions, the concentration of DMSO never exceeded 0.1% (w/v).

MCF-7 Cytotoxicity Assay

The MCF-7 cells were seeded in a 96-well plate at a density of 10 × 103 cells/well. Cells were allowed to attach for 24 h at 37 °C before the medium was removed and replaced with 100 μL of medium containing the appropriate Paclitaxel concentration (0.1 μM, 1 μM, 10 μM, 25 μM, 50 μM). 0.5% DMSO and growth medium without addition of Paclitaxel (0 μM, Fig. 6d) were used as vehicle controls. Four replicate wells were used for each drug concentration and controls. Cells were treated for 24 h at 37 °C before cell viability was determined using a PrestoBlue assay; 100 μL of PrestoBlue solution (10% in medium) was added to each well and the plate was incubated at 37 °C for 1 h. After incubation, the plate was read using a FLUOstar Omega plate reader with the excitation/emission wavelengths set at 544/590 nm and the PrestoBlue response compared to untreated cells. The percentage of cell viability was calculated using untreated cells as a maximal proliferation.

MCF-7 Cells Cultured in PS Well-Plates Treated with Paclitaxel

The MCF-7 cells were plated into sterile polystyrene culture dishes (Corning 35 mm TC-treated culture dishes, product number 430165) at a density of 6 × 105 cells/dish and incubated at 37 °C for 24 h. Afterwards, the media was removed and cells were incubated with 1.5 mL of media containing the appropriate Paclitaxel concentration (10 μM and 50 μM) for 4 h and 24 h at 37 °C. As a control group, MCF-7 cells maintained in growth media were used. After the required incubation time, cells were fixed in 4% (w/v) paraformaldehyde at room temperature for 10 min and stored in PBS before being transferred under the Raman microscope.

Statistical Analysis

The results are given as mean ± SD. Statistical analysis was performed with GraphPad Prism 7 software using one-way analysis of variance (ANOVA) followed by Tukey's *t*-test for multiple comparisons. $^{*}P < 0.05$ was considered significant, $^{**}P < 0.001$ was considered highly significant. $P > 0.05$ was considered not statistically significant.

Raman Data Processing

All data processing, optical aberration, and S/N ratio modeling was done in Matlab (The Mathworks Inc.) using custom home built functions. Raman shift axis calibration was carried out using a polystyrene spectrum and a third-order polynomial fit to six bands. The raw hyperspectral data were first processed to remove cosmic ray spikes. Following this, automated background subtraction of the full spectral window was performed using the method used by Lieber and Mahadevan-Jansen[24] with a third-order polynomial fit, and automated polymer signal removal using the method of Beier and Berger[25] using ten iterations for algorithm optimization. Following this, noise reduction based on singular value decomposition (SVD) using principal component analysis (PCA) was carried out, with the maximum number of PCs decided on a cell-by-cell dataset basis.[8] Band-area maps were then generated by integrating the intervals 760–800 cm^{-1} for the 788 cm^{-1} nucleic acids O–P–O stretch band, 1400–1510 cm^{-1} for the 1450 cm^{-1} CH_2 stretch (predominantly lipid) band, and 1585–1700 cm^{-1} for the 1650–1660 cm^{-1} amide I protein band (a local linear baseline was subtracted).

Results and Discussion

Theoretical Model for Estimating Signal-to-Noise Ratio in Raman Spectroscopy Measurements of Single Cells Cultured on a Polymer Substrate

In an idealized case when optical aberrations are negligible, a focused laser used for Raman spectroscopy excitation will have an axial intensity distribution in the focal region that will be diffraction-limited at best. The depth of field in this case is defined as $\Delta z = 2n\lambda/NA^2$, where n is the refractive index of the medium, λ is the wavelength of the light, and NA the numerical aperture of the objective lens. For Raman excitation with 785 nm lasers, Δz will be between 1–2 μm when using an immersion objective with $NA = 1.2$. For Raman measurements of fixed cells in phosphate buffered saline (PBS) with typical thickness 1–10 μm, this resolution is sufficient for maximizing the amount of total incident power which will be focused inside the cell volume. For a cell located on a polymer substrate, this would also mean that the undesirable signal generated from the polymer and the aqueous solutions (culture medium or PBS) would be minimized. However, in real measurements Δz will increase because of optical aberrations, thus increasing the contribution from the substrate and PBS. Thus, the total measured Raman signal would then contain contributions from the cell, polymer, and aqueous solution (the contribution for the cell will decrease), as a proportion of the incident laser will be focused outside the cell. As polymers typically generate more intense Raman scattering than cells, their signal would be expected to

rapidly increase when the optical aberrations are more pronounced.

If the spectra of the polymer and aqueous solution are known, they can be subtracted away from the total signal to retrieve the spectrum of the cell in principle. However, the associated shot-noise components will remain, placing limitations on the relative strength of the cell signals that can be retrieved. To see this explicitly, consider $S(\bar{\nu})$, the total signal measured at a Raman CCD pixel (dependent on Raman wavenumber $\bar{\nu}$), which for the case of a cell–polymer sample can be written

$$S(\bar{\nu}) = \sum_i S_i^{\text{measured}}(\bar{\nu}) + N^{\text{dark}} + N^{\text{read}} \tag{1}$$

where N^{dark} is the CCD pixel dark current noise, N^{read} is the CCD readout noise, and S_i^{measured} are the measured Raman photons originating from different materials in the sampling region (i = polymer, cell, PBS, etc.). The Raman photons can be expressed as the combination of an idealized photon expectation value and shot noise component, for example $S_{\text{polymer}}^{\text{measured}}(\bar{\nu}) = S_{\text{polymer}}^{\text{ideal}}(\bar{\nu}) + N_{\text{polymer}}^{\text{shot}}(\bar{\nu})$, where the shot noise $N_{\text{polymer}}^{\text{shot}}$ can also be written as the square root of a Poisson random number $(Poiss[x])$ generated from a distribution where $S_{\text{polymer}}^{\text{ideal}}$ is the expectation (lambda) value, i.e., $N_{\text{polymer}}^{\text{shot}} = \sqrt{Poiss[S_{\text{polymer}}^{\text{ideal}}]}$ (likewise for other signals). Thus, the total signal can be rewritten as

$$S(\bar{\nu}) = \sum_i \left(S_i^{\text{ideal}}(\bar{\nu}) + \sqrt{Poiss[S_i^{\text{ideal}}(\bar{\nu})]} \right) + N^{\text{dark}} + N^{\text{read}} \tag{2}$$

For broad background contributions in Raman spectra, simple polynomial fitting is most commonly used,[24] while more recently automated routines have been developed for removing specific background signals from a known source using a reference input spectrum, which can be applied in this case to remove the component $S_{\text{polymer}}^{\text{ideal}}$ and $S_{\text{PBS}}^{\text{ideal}}$.[25] However, the shot noise, N_i^{shot} associated with S_i^{ideal}, is inherently stochastic and thus cannot be removed deterministically. This places a limit on the possibility for recovery of the Raman spectrum of the cell. This can be seen when considering the S/N ratio of the polymer–PBS-subtracted spectrum for a cell–polymer system is

$$SNR(\bar{\nu}) = \frac{S_{\text{cell}}^{\text{ideal}}(\bar{\nu})}{\sqrt{Poiss\left[S_{\text{polymer}}^{\text{ideal}}(\bar{\nu})\right]} + \sqrt{Poiss\left[S_{\text{cell}}^{\text{ideal}}(\bar{\nu})\right]} + \sqrt{Poiss\left[S_{\text{PBS}}^{\text{ideal}}(\bar{\nu})\right]} + N^{\text{dark}} + N^{\text{read}}} \tag{3}$$

which is also dependent on $\bar{\nu}$, as $S_{\text{polymer}}^{\text{ideal}}$, and $S_{\text{PBS}}^{\text{ideal}}$ vary in intensity with Raman shift. Thus, for wavenumber bands in which there exist large polymer/PBS Raman scattering signals, the associated shot noise will dominate the noise term, and the S/N ratio will be degraded. It is therefore possible that after subtraction, bands assigned to cellular biomolecules at positions where polymers have no bands (thus low shot noise) should be detectable, while cell bands that overlap strong polymer bands (high shot noise) would be hard to detect. The minimization of the axial spread of laser intensity, such as when using diffraction limited optics, will achieve the maximum S/N ratio of the measured cell spectrum as the relative strength of $S_{\text{cell}}^{\text{ideal}}$ is highest with respect to $S_{\text{polymer}}^{\text{ideal}}$.

Spherical Aberration in Raman Microspectroscopy of a Three-Layer System

For the Raman spectroscopy measurements of cells on polymers shown in Fig. 1a and 1b, the use of the microscope objectives in each case deviates from the ideal/intended operating conditions. It is thus useful to predict these deviations to understand current measurement limitations and potentially suggest routes forward for improvement.

Previous work by Everall has demonstrated the need for careful consideration of the effects of spherical aberration in Raman microscopy.[26,27] In particular, the broadening of the laser intensity along the optical axis due to spherical aberration is expected to result in Raman scattering from unwanted parts of the sample, in this case the polymer substrates and PBS. For cells cultured on PLGA measured through quartz (using the setup in Fig. 1a), the objective is focused away from the coverslip material to reach the cells adhered to the polymer. For cells on PS (using the setup in Fig. 1b), the oil immersion objective is intended for use with 0.5–1.0 mm of fused quartz ($n_2 = 1.473$), not PS ($n_2 = 1.579$), which results in a significant refractive index mismatch at the interface $n_2 \leftrightarrow n_3$ (oil immersion: $n_1 = 1.459$).

In order to estimate the aberrations in each case, we consider a model similar to that introduced by Everall,[26] but extended to a three-layer system with liquid-immersion objectives. For an objective with numerical aperture

$$NA = n_1 \sin \theta_{\max} \tag{4}$$

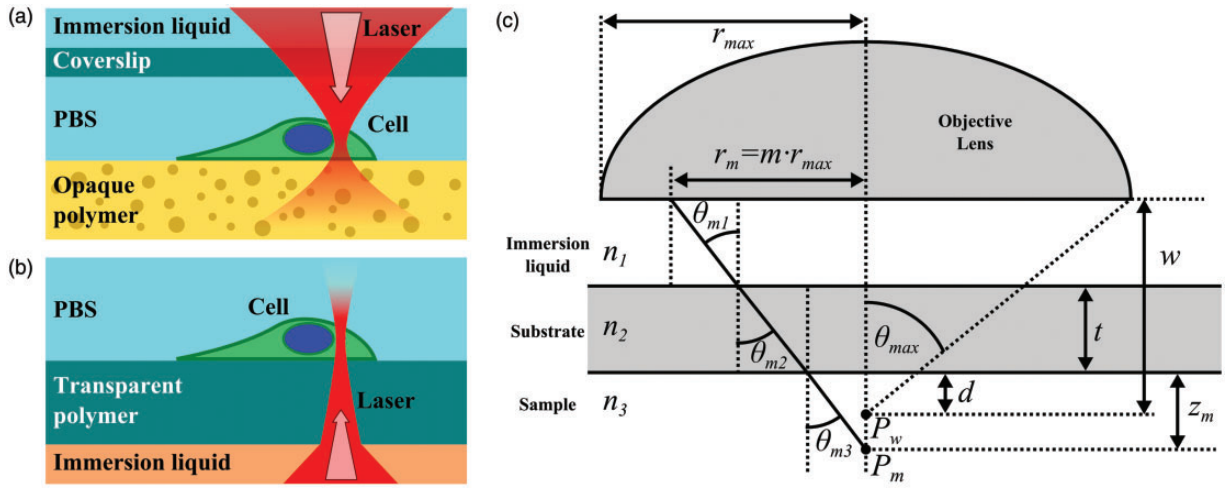

Figure 1. General schemes for approaching Raman spectroscopic measurement of cells on polymers, with (a) the case that an optically thick/opaque polymer is used and cells are measured using a dipping or immersion objective through a coverslip, and (b) the case when a transparent polymer is used and cells are measured directly through it using an immersion objective. (c) Parameters for ray tracing analysis of optical aberrations in Raman excitation when using high-NA immersion objectives through a substrate material to a biological sample (an extension of the model by Everall[26,27]); r_{max} is the maximum radius from which rays will leave the objective at the angle θ_{max} (related to *NA*); *m* is the fraction of r_{max} (radius r_m) from the center of the objective ($0 \leq m \leq 1$); n_1 is the refractive index of the immersion liquid, n_2 the substrate, and n_3 the sample; *t* is the substrate thickness, and *w* the objective working distance; *d* is the distance into the sample all rays will reach (at point P_w) in the absence of refractive effects, and z_m the depth a ray will travel to reach point P_m, which originated from the objective at r_m with angle θ_{m1}. The angles θ_{m1}, θ_{m2}, and θ_{m3} can be related using Snell's law.

the maximum radius of the objective lens from which laser illumination is possible (shown in Fig. 1c) is

$$r_{\max} = \frac{w \cdot NA}{\sqrt{n_1^2 - NA^2}} \tag{5}$$

A ray emerging at a point r_m away from the center of the objective with angle θ_{m1} (shown in Fig. 1c) will cross the objective optical axis at point P_m at a depth z_m below the $n_2 \leftrightarrow n_3$ interface, which can be expressed as

$$z_m = \frac{a_3(m)}{a_1(m)}\left(t\left(1 - \frac{a_1(m)}{a_2(m)}\right) + d\right) \tag{6}$$

where

$$a_k(m) = \sqrt{n_k^2 \delta n_1^2 + m^2 NA^2\left(n_k^2 - n_1^2\right)} \tag{7}$$

and

$$\delta n_k = \sqrt{n_k^2 - NA^2} \tag{8}$$

with the label $k = 1, 2, 3$ referring to the particular material refractive index (derivation in the Supplemental Material). Note that in the limiting case when $t \to 0, n_1 \to 1$, $n3 \to n$, these equations return exactly to the form shown by Everall for a two-layer system.[26]

The depth of field can then be written as $\Delta z = z_1 - z_0$, which using Eq. 6 becomes

$$\Delta z = t \cdot [c_{31} - c_{32}] + d \cdot c_{31} \tag{9}$$

where

$$c_{ij} = \left(\frac{\delta n_i}{\delta n_j} - \frac{n_i}{n_j}\right) \tag{10}$$

Similar to Everall,[26] in order to relate this to an axial intensity distribution, we assume a Gaussian beam entering the back aperture of the objective in each case, with intensity described by $I_m = I_0 e^{-m^2/\phi^2}$, with the fill factor $\phi = 1$ and I_0 the total incident intensity. This distribution is then weighted by *m* such that the axial intensity distribution is described by $m \cdot I(m)$.[26]

These equations tell us some important things for each measurement case. For the case of Fig. 1a, there will be a layer of PBS between the quartz coverslip and the cells that typically has a thickness of the order 30 μm for the

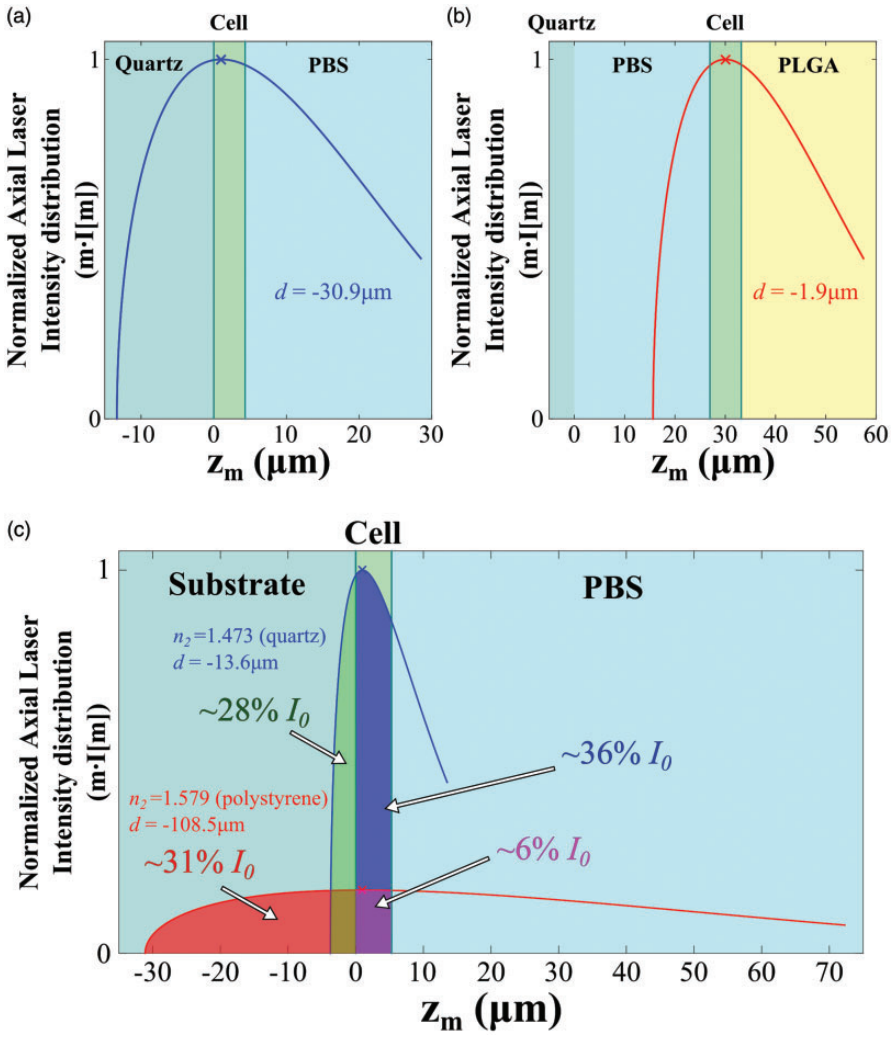

Figure 2. Spherical aberration of laser intensity in the two measurement configurations obtained from Eq. 6. Curves are normalized to be constant area (total intensity I_0). Top images show the axial spread for the PLGA-cell measurements (setup in Fig. 1a) when the (a) ideal and (b) actual (approximately 30 μm deep) measurement configurations are used. Note: the objective used for these measurements has a correction collar which will actually improve the axial spread shown here closer to the diffraction limit (parameters used: $NA = 1.2$, $n_1 = 1.33$ water, $n_2 = 1.473$ quartz, $n_3 = 1.33$ PBS, $t = 0.18$ mm). (c) Axial intensity distribution for the PS-cell measurements (setup in Fig. 1b) when d is varied such that the maximum of the laser intensity distribution is 1 μm above the substrate into the cell (blue line: quartz substrate, red line: PS substrate, parameters used: $NA = 1.2$, $n_1 = 1.459$ oil, $n_2 = 1.579$ polystyrene and $n_2 = 1.473$ quartz, $n_3 = 1.4$ cell, $t = 1$ mm).

experiments described later with ovarian cancer cells on PLGA films. This means that as $n_1 \approx n_3$, then $c_{31} \approx 0$, thus there is negligible change in the depth of field as a function of d as seen in Fig. 2a and 2b. The only remaining term causing aberration depends on t, which can be ignored, as the objective used for the corresponding experiment has a coverslip correction collar (which is not accounted for in this simple model). Therefore, it is reasonable to assume that the tight axial resolution will be maintained when focusing through 30 μm of PBS to reach cells for the Raman measurement. Nevertheless, the shot noise in the spectrum would be expected to increase because of the Raman background signal of the PLGA substrate.

For the setup in Fig. 1b, when the quartz substrate is substituted for PS of comparable thickness t, each interface will have a refractive index mismatch leading to significant spherical aberration. This can clearly be seen in Fig. 2b where the axial intensity distribution is plotted for two "measurement" cases, chosen for d when laser intensity distribution is at a maximum at 1 μm deep into a cell. It can be seen that when the quartz substrate is used, an estimated 36% of the total incident power will be focused inside the cell, with 28% in the quartz, and remaining 36% in the PBS. However, when substituted with a PS substrate of the same thickness d, the spherical aberration results in a much broader axial distribution, with only about 6% of the

incident laser intensity focused within the cell, with 31% focused inside the PS and 63% in the PBS. The ideal signals from each material at each wavenumber will be proportional to their respective Raman cross-sections ($\sigma_i(\bar{\nu})$), the concentration of Raman scattering moieties (c_i), sampling volume (V_i), and the laser intensity ($I_i = p_i \cdot I_0$, where p_i is the proportion of the incident laser (I_0) focused within the labeled region)

$$S_i^{\text{ideal}}(\bar{\nu}) \propto \sigma_i(\bar{\nu}) \cdot c_i \cdot V_i \cdot p_i \cdot I_0 \tag{11}$$

For the case in which the polymer and PBS shot noise are the dominant noise contributions, Eq. 3 can be rewritten explicitly as

$$SNR(\bar{\nu}) \propto \frac{\sigma_{\text{cell}}(\bar{\nu}) \cdot c_{\text{cell}} \cdot V_{\text{cell}} \cdot p_{\text{cell}} \cdot I_0}{\left\{\sqrt{Poiss[\sigma_{\text{polymer}}(\bar{\nu}) \cdot c_{\text{polymer}} \cdot V_{\text{polymer}} \cdot p_{\text{polymer}} \cdot I_0]} + \sqrt{Poiss[\sigma_{PBS}(\bar{\nu}) \cdot c_{PBS} \cdot V_{PBS} \cdot p_{PBS} \cdot I_0]}\right\}} \tag{12}$$

Equation 12 illustrates several important considerations for maximizing *SNR* when measuring cells on polymers. First, the proportion of the total incident laser intensity focused within the cell (p_{cell}) must be maximized, while also minimizing (p_{polymer}) and (p_{PBS}). However, it can be seen in Fig. 2c that (p_{polymer}) and (p_{quartz}) are very similar, but in this case the major difference will be related to the difference between σ_{polymer} $(\bar{\nu})$, c_{polymer}, and V_{polymer} and their quartz counterparts. As a practical example, consider the phenyl ring breathing mode at 1003 cm^{-1}, which occurs in cellular proteins and PS but not quartz; thus, σ_{quartz} (1003) will be negligible, while σ_{polymer} (1003) $\approx \sigma_{\text{cell}}$ (1003). However, it is reasonable to assume that the phenyl rings present in the PS substrate will have a much greater concentration than those present in phenylalanine within proteins in the cell, i.e., $c_{\text{polymer}} \gg c_{\text{cell}}$. Furthermore, although $p_{\text{polymer}} \approx p_{\text{quartz}}$, the volume of the substrate sampled (i.e., axial spread within this region) is not the same, with Fig. 2c implying that $V_{\text{polymer}} \gg V_{\text{quartz}}$. For a given substrate, σ_i and c_i will be constant, and thus the S/N ratio can only be controlled experimentally by minimizing both V_i and p_i in the substrate. The same reasoning can also be applied to the PBS/other aqueous solutions and also other wavenumbers.

OVCAR3 Cells Cultured on Nanopatterned PLGA Films

The ability of biomaterials to alter cancer cell behavior will be influenced by their surface properties, i.e., chemical nature of the biomaterials and surface topography. Previous studies in the literature have been carried out with various topographies including grooves, wells, pits, and protrusions of diverse chemical structures.[22] The results show that cells including cancer cells respond to nano- and micro-textured biomaterial surfaces, where changes in cell adhesion, proliferation, orientation, alignment, migration, and morphology were all observed. These textured biomaterials may mimic in vivo microenvironments, and thus enable modeling of cell–cell and cell–extracellular matrix interactions and modulating of cell-surface interactions.

Here, we use OVCAR3 cells adhered to nanopatterned PLGA films as an example of the setup outlined in Fig. 1a. The PLGA films containing cells were placed on a quartz coverslip and measured on an inverted Raman microscope after the liquid layer between the quartz and PLGA film had equilibrated to roughly 30 μm (typically after 20 min). Maps were acquired within 2–3 h of being seeded onto the films, due to degradation of the PLGA structure in PBS, and were

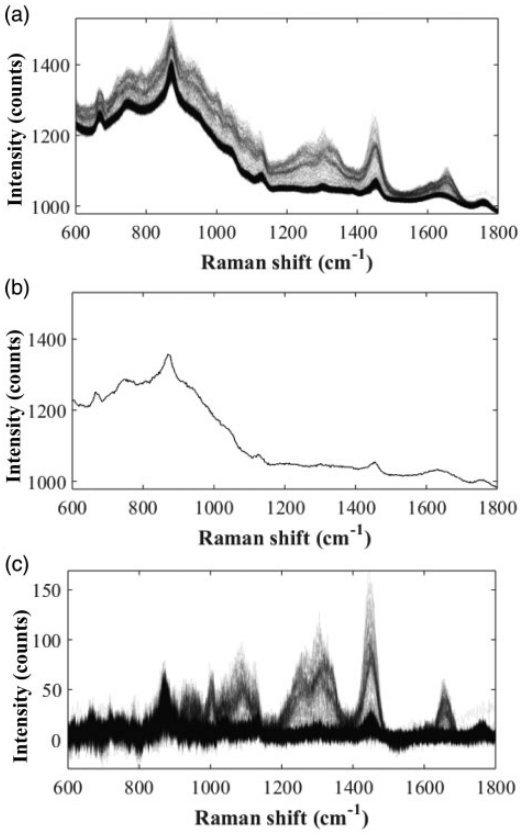

Figure 3. Demonstration of background removal procedure for a Raman map of an OVCAR3 cell on a PLGA film. (a) Example of raw Raman map data (after cosmic ray removal, spectra plotted with 5% transparent lines to highlight variation in the data set, 2 s per spectrum). (b) PLGA spectrum used for library-based background subtraction (mean of five background pixels in hyperspectral data set). (c) Raman map spectra after automated background subtraction using the spectrum in (b) as a PLGA reference.

taken with 2 s/pixel acquisition time in steps of 2 μm. Roughly ten cells were measured on each of the samples (non-textured and hemispherical protrusion shaped nano-textured PLGA films).

Figure 3a shows that for certain samples, this experimental configuration results in raw spectra in which Raman bands from the cell are immediately observable even without background subtraction. At this stage, direct application of PCA on the raw data identifies loadings with clear Raman features associated with cells, typically within the first five PCs (often the second). As the spectra of PLGA and OVCAR3 are of a similar intensity, the background subtraction process (using the reference spectrum shown in Fig. 3b) results in spectra with minimal residual interference from the shot noise produced by the strongest PLGA bands at 870 cm^{-1} and 1450 cm^{-1}, as can be seen in

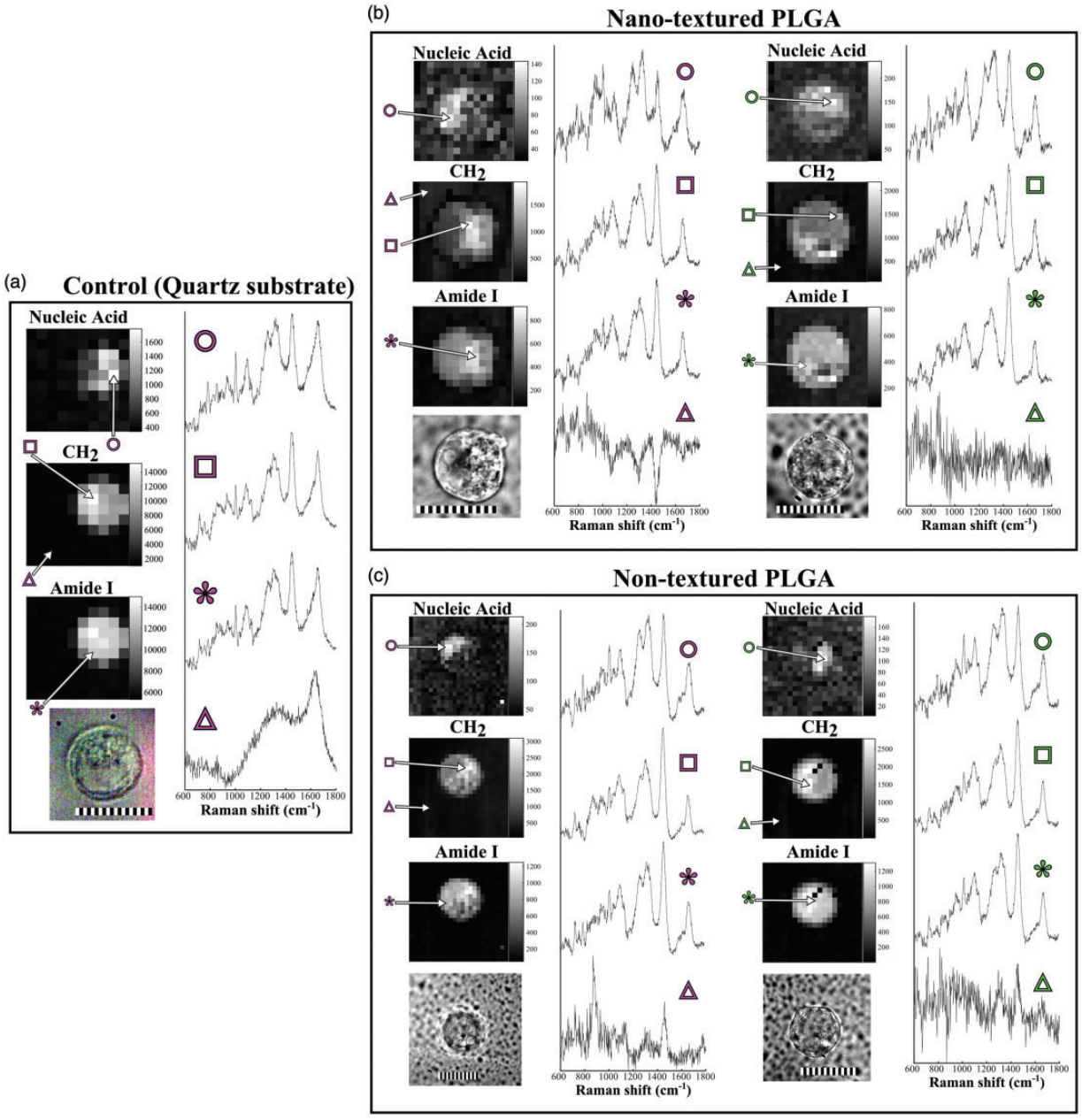

Figure 4. (a) Control measurement of OVCAR3 measured directly on quartz with no PLGA (5 s per spectrum, 4 μm step size). (b) OVCAR3 cells on nanotextured PLGA films measured through a quartz substrate. (c) OVCAR3 cells on non-textured PLGA films measured through a quartz substrate. For each cell shown, the Raman map generated by band areas is shown for nucleic acids (788 cm^{-1}), lipids (CH_2, 1450 cm^{-1}), and protein (amide I, 1655 cm^{-1}), with several example spectra from the indicated image locations (after background subtraction and SVD noise-reduction) and a bright-field image (scale bars 20 μm).

Fig. 3c. Figure 4 shows that further noise reduction by singular value decomposition (SVD)–reconstruction of the first 8–10 principal components, the OVCAR3 cell spectra can clearly be seen against the almost flat background spectra, with only relatively small residual PLGA spectral components. After processing, the cell Raman spectra from the PLGA surface are comparable with those of the same cells measured on a quartz substrate (Fig. 4a).

After polymer-background correction and SVD noise reduction, Raman maps based on band area can be obtained to show the distribution of biomolecules in the OVCAR3 cells. In each case shown in Fig. 4, the nucleus is clearly

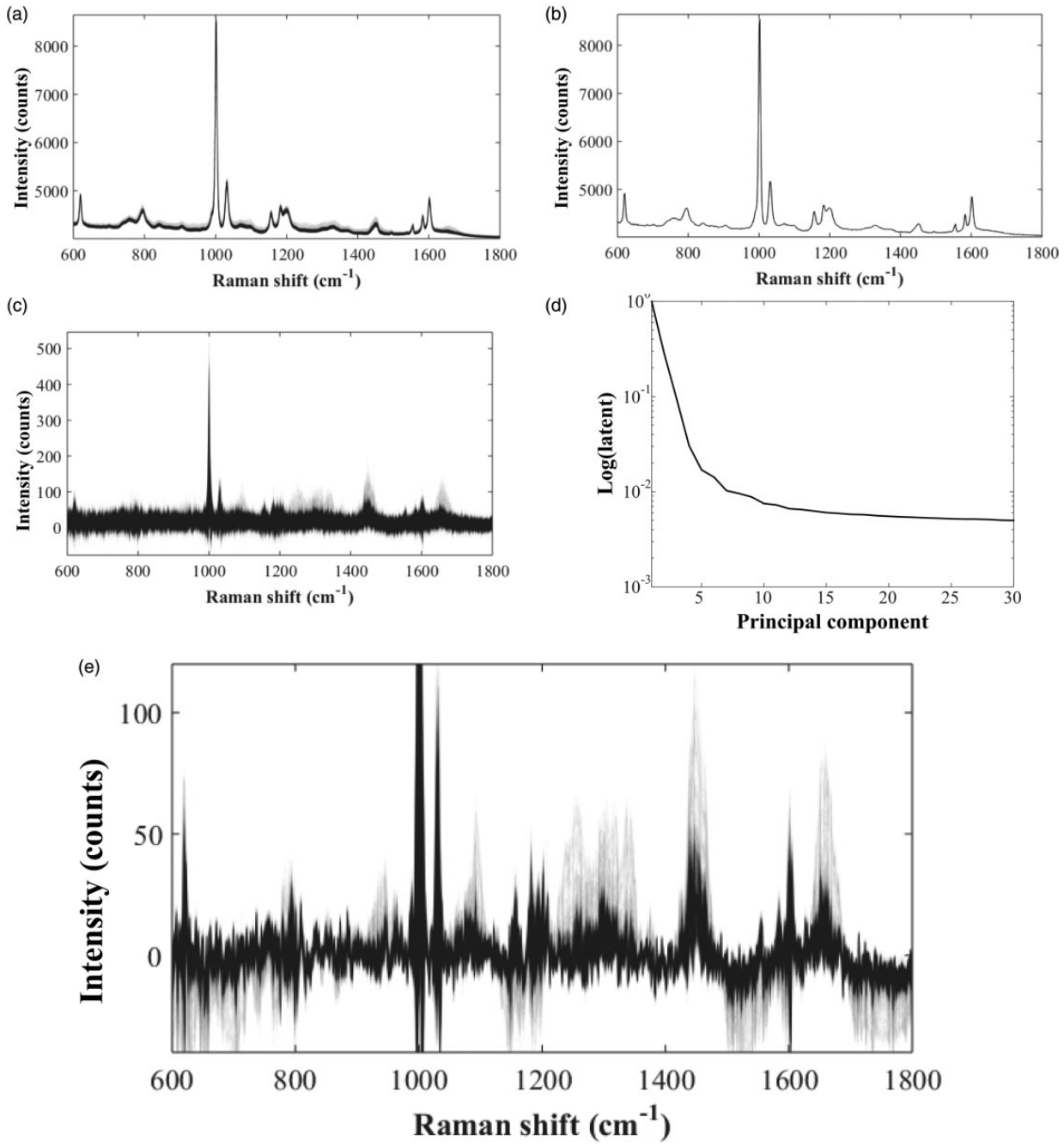

Figure 5. Demonstration of background removal procedure for a Raman map of an MCF-7 cell on a PS substrate. (a) Example of raw (after cosmic ray removal) Raman map data, showing dominance of PS signal. (b) Polystyrene spectrum used for library-based background subtraction (mean of five background points on map). (c) Map spectra after automated background subtraction. (d) Latent plot of PCA components of the data in (c). (e) Singular value decomposition noise-reduced spectra using PCs 1–20 (spectra plotted with 5% transparent lines to highlight variation in the data set, residual PS bands are cropped to emphasize the presence of cell bands).

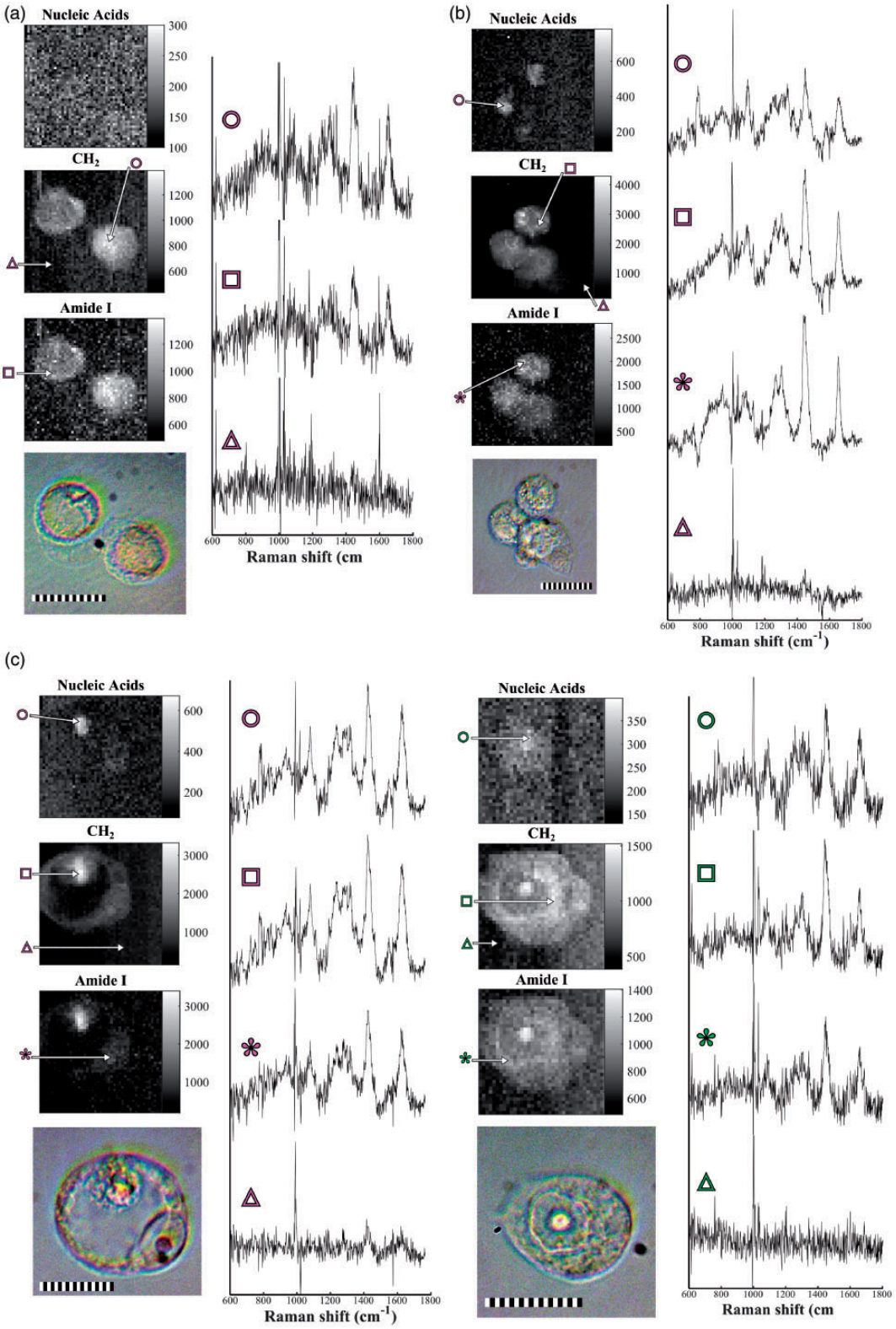

Figure 6. Raman microspectroscopy of Paclitaxel-treated MCF-7 cells on PS. Band-area images of MCF-7 cells fixed after (a) 4 h with 10 μM paclitaxel solution, (b) 24 h with 10 μM paclitaxel solution, and (c) 24 h with 50 μM paclitaxel solution. Scale bars in all accompanying bright field images is 20 μm.

distinguishable from the rest of the cell using the 788 cm^{-1} band assigned to nucleic acids (O–P–O stretching). The amide I band map also reveals the protein distribution throughout the cell with low background contribution. Even in regions where PLGA-associated bands overlap with cell-associated bands, such as at 1450 cm^{-1}, the cell signal is of sufficient quality for producing low background noise images.

These results indicate that this particular experimental arrangement minimizes Raman sampling of the PLGA material, with the majority of the incident laser focused within the cell, leading to relatively high-fidelity spectra able to be retrieved after background subtraction. This agrees well with the assertion in the Spherical Aberration in Raman Micro-Spectroscopy of a Three-Layer System section that an objective with an aberration correction collar focused several tens of micrometers into PBS will essentially have the same axial laser intensity distribution as at the quartz surface (see Fig. 2a and 2b).

MCF-7 Cells Cultured in Polystyrene Well-Plates Treated with Paclitaxel

Raman microspectroscopy has previously been used for various examples of anti-cancer drug delivery to single cells, for both drug localization and monitoring the effects on the cells themselves.[15–17] One particular example is the use of paclitaxel in treating breast cancer cells (MCF-7). Paclitaxel induces tubulin polymerization, halting the cell cycle, and causing mitotic arrest.[28] Previous RMS studies with MCF-7/paclitaxel have been performed on CaF_2 substrates,[17] whereas here we demonstrate we can measure the same system on PS substrates routinely used in pharmaceutical research.

Figure 5a shows that typically for this measurement configuration, the PS spectrum overwhelms the MCF-7 cell spectrum such that it is not possible to observe the latter directly, which is unsurprising as Fig. 2c indicates that roughly five times more of the incident laser power is likely to be focused within the PS than the cell due to spherical aberration. After similar processing steps to those shown in Fig. 3 (shown in Fig. 5b–d, see Materials and Methods for details), some bands assigned to the MCF-7 cell spectrum can be observed in Fig. 5e. In this case, there is significant residual shot noise at wavenumbers containing strong PS bands after subtraction, essentially ruling out these regions for detection of cell Raman bands (e.g., phenyl ring breathing mode at 1003 cm^{-1}). However, Raman bands that occur in spectral regions with weak or no PS bands are consistently observable, such as the CH_2 stretch, amide I, and amide III modes. Cell-like Raman features were readily observed for a majority of samples after applying PCA, but often contained significant noise resulting in difficulty for band-area imaging.

The ability to measure hyperspectral Raman images of cells exposed anti-cancer drugs and detect early stages of apoptosis is demonstrated in Fig. 6. For images obtained for cells treated with lower drug concentrations and short exposure times (4 h, 10 μM paclitaxel, Fig. 6a), the 788 cm^{-1} band was below the detection limit. However, at 24 h treatment, for both 10 μM and 50 μM (Fig. 6b and 6c, respectively), most cells were observed to have concentrated regions of nucleic acids, particularly for concentrations of 50 μM, where a highly localized nucleic acid/protein signal

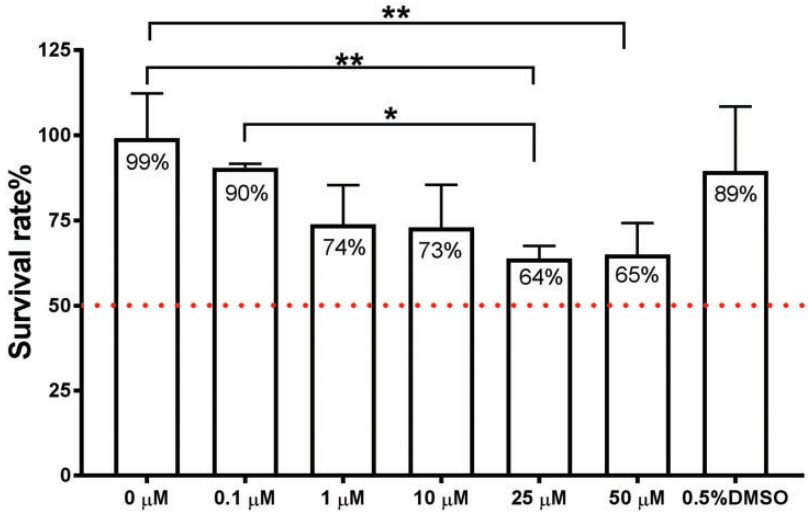

Figure 7. MCF-7 viability (measured using PrestoBlue assay, see Materials and Methods for details) for paclitaxel treatment and DMSO/no drug controls after 24 h. * indicates P value < 0.05 (considered significant), ** indicates P-value < 0.001 (considered highly significant).

was observed in several cases. This is often associated with the early stages of apoptosis where DNA condensation occurs and lipid structures collect at the edges of cells. DNA condensation has been previously reported in Raman hyperspectral imaging on other cell lines,[9–11] but only for cells cultured on low-background substrates such as MgF_2 and CaF_2. The results of the viability tests for MCF-7 cells exposed to paclitaxel (shown in Fig. 7) confirmed a drop by 26% and 34% 24 h after treatment with 10 μM and 50 μM paclitaxel, respectively.

Although we show that high-quality hyperspectral Raman images can be obtained for cells cultured in routine cell culture PS plates, it is clear that these measurements are close to the detection limit. Nevertheless, the link between the quality of the Raman spectra and the optical aberrations provide us scope for future improvements. The results in Fig. 2c indicate that only $p_{cell} = 6\%$ of the incident laser power (~3 mW in this case) will actually be focused within the cell, compared with 28% when the aberrations are minimized by using a quartz substrate. If the measurement conditions can be modified to reduce the aberration when using the PS substrate, this would increase the fraction of the laser intensity exciting the Raman scattering by the biomolecules within the cells, leading to improved S/N ratio Raman spectra.

Conclusion

We have demonstrated the ability to measure Raman hyperspectral images of cells cultured on polymer substrates, based on two configurations typically encountered in biomedical sciences and engineering. The quality of the Raman spectra, in terms of S/N ratio, obtained after the subtraction of the Raman signal of the polymer substrate depend on the experimental configuration, as these often induce optical aberrations that alter the axial profile of the laser. The Raman spectra retrieved from OVCAR3 cells on PLGA films through a thin quartz coverslip were of sufficient quality to consistently map the 788 cm^{-1}, 1450 cm^{-1}, and 1655 cm^{-1} (nucleic acid, CH_2, and amide I) bands, with spectra of high S/N ratio routinely achievable. This configuration can be commonly encountered when studying the interaction of cells with various polymer materials, such as tissue engineering and stem cells bioengineering. The measurement of MCF-7 cells cultured in PS culture plates led to lower S/N Raman spectra of the cells, as the optical aberrations with much more pronounced. These aberrations led to a higher level of shot noise caused by the strong PS Raman bands, concomitant with a reduction in the Raman signal from the cellular molecules caused by the decrease laser intensity within the cell volume. Despite these effects, many of the processed Raman hyperspectral data sets could identify the CH_2 and amide I bands, and occasionally high concentrations of nucleic acids. This was most evident in the case of MCF-7 cells exposed to the anti-cancer drug paclitaxel, which is known to induce apoptosis. Despite the high noise level caused by the PS signal, the induced DNA condensation associated with the early stages of drug-induced apoptosis led to an increase in the intensity of the 788 cm^{-1} Raman band, allowing mapping of the DNA with high accuracy. Other hallmarks of apoptosis, such as increase in lipid droplets in the cell cytoplasm, were also observed. Both measurements are made possible by using highly confocal detection with immersion objectives, and an automated background removal routine that uses a library polymer spectrum as described in Beier and Berger.[25] While it is clear that the Raman spectra of cells measured in the presence of a polymer will always be negatively affected by the noise limitations described, we have demonstrated that it is indeed possible to retrieve useful information relevant to biomedical applications. With these examples it is now feasible that RMS may be used to provide complementary information for cells measured in more complex environments than was previously thought achievable. Furthermore, the theoretical model developed in this paper also indicates that the measurements on cells cultured in PS culture plates could be optimized further by accounting for the significant refractive index mismatch of the quartz-matched immersion oil and PS substrate in current measurements, resulting in a tighter axial laser focus.

Acknowledgments

The authors thank Professor Morgan Alexander for providing access to cell cultures and PLGA/PS materials. This work was supported by the Engineering and Physical Sciences Research Council [grant numbers EP/M506588/1, EP/L025620/1].

Conflict of Interest

The authors report there are no conflicts of interest.

Supplemental Material

All supplemental material mentioned in the text, consisting of a derivation of spherical aberration formula, a scheme, and a figure, is available in the online version of the journal.

References

1. D.W. Shipp, F. Sinjab, I. Notingher. "Raman spectroscopy: Techniques and Applications in the Life Sciences". Adv. Opt. Photonics. 2017. 9(2): 315–428.
2. B. Kann, H.L. Offerhaus, M. Windbergs, C. Otto. "Raman Microscopy for Cellular Investigations: From Single Cell Imaging to Drug Carrier Uptake Visualization". Adv. Drug Delivery Rev. 2015. 89: 71–90.
3. G.J. Puppels, F.F.M. De Mul, C. Otto, J. Greve, et al. "Studying Single Living Cells and Chromosomes by Confocal Raman Microspectroscopy". Nature. 1990. 347(6290): 301.
4. C. Krafft, T. Knetschke, A. Siegner, R.H. Funk, et al. "Mapping of Single Cells by Near Infrared Raman Microspectroscopy". Vib. Spectrosc. 2003. 32(1): 75–83.
5. K. Hamada, K. Fujita, N.I. Smith, M. Kobayashi, et al. "Raman Microscopy for Dynamic Molecular Imaging of Living Cells". J. Biomed. Opt. 2008. 13(4): 044027.

6. L. Ashton, K.A. Hollywood, R. Goodacre. "Making Colourful Sense of Raman Images of Single Cells". Analyst. 2015. 140(6): 1852–1858.
7. R. Boitor, F. Sinjab, S. Strohbuecker, V. Sottile, et al. "Towards Quantitative Molecular Mapping of Cells by Raman Microscopy: Using AFM for Decoupling Molecular Concentration and Cell Topography". Faraday Discuss. 2016. 187: 199–212.
8. N. Uzunbajakava, A. Lenferink, Y. Kraan, E. Volokhina, et al. "Nonresonant Confocal Raman Imaging of DNA and Protein Distribution in Apoptotic Cells". Biophys. J. 2003. 84(6): 3968–3981.
9. A. Zoladek, F.C. Pascut, P. Patel, I. Notingher. "Non-Invasive Time-Course Imaging of Apoptotic Cells by Confocal Raman Micro-Spectroscopy". J. Raman Spectrosc. 2011. 42(3): 251–258.
10. M. Okada, N.I. Smith, A.F. Palonpon, H. Endo, et al. "Label-Free Raman Observation of Cytochrome c Dynamics During Apoptosis". Proc. Natl. Acad. Sci. U. S. A. 2012. 109(1): 28–32.
11. K. Czamara, F. Petko, M. Baranska, A. Kaczor. "Raman Microscopy at the Subcellular Level: a Study on Early Apoptosis in Endothelial Cells Induced by Fas Ligand and Cycloheximide". Analyst. 2016. 141(4): 1390–1397.
12. H.G. Schulze, S.O. Konorov, N.J. Caron, J.M. Piret, et al. "Assessing Differentiation Status of Human Embryonic Stem Cells Noninvasively Using Raman Microspectroscopy". Anal. Chem. 2010. 82(12): 5020–5027.
13. F.C. Pascut, T.H. Goh, N. Welch, L.D. Buttery, et al. "Noninvasive Detection and Imaging of Molecular Markers in Live Cardiomyocytes Derived from Human Embryonic Stem Cells". Biophys. J. 2011. 100(1): 251–259.
14. A. Ghita, F.C. Pascut, M. Mather, V. Sottile, I. Notingher. "Cytoplasmic RNA in Undifferentiated Neural Stem Cells: A Potential Label-Free Raman Spectral Marker for Assessing the Undifferentiated Status". Anal. Chem. 2012. 84(7): 3155–3162.
15. S.F. El-Mashtoly, D. Petersen, H.K. Yosef, A. Mosig, et al. "Label-Free Imaging of Drug Distribution and Metabolism in Colon Cancer Cells by Raman Microscopy". Analyst. 2014. 139(5): 1155–1161.
16. S.F. El-Mashtoly, H.K. Yosef, D. Petersen, L. Mavarani, et al. "Label-Free Raman Spectroscopic Imaging Monitors the Integral Physiologically Relevant Drug Responses in Cancer Cells". Anal. Chem. 2015. 87(14): 7297–7304.
17. H. Salehi, L. Derely, A.G. Vegh, J.C. Durand, et al. "Label-Free Detection of Anticancer Drug Paclitaxel in Living Cells by Confocal Raman Microscopy". Appl. Phys. Lett. 2013. 102(11): 113701.
18. H.M. Naemat, R.A. Elsheikha, I. Boitor, Notingher. "Tracing Amino Acid Exchange During Host-Pathogen Interaction by Combined Stable-Isotope Time-Resolved Raman Spectral Imaging". Sci. Rep. 2016. 6: 20811.
19. L.T. Kerr, H.J. Byrne, B.M. Hennelly. "Optimal Choice of Sample Substrate and Laser Wavelength for Raman Spectroscopic Analysis of Biological Specimen". Anal. Methods. 2015. 7(12): 5041–5052.
20. K. Ramoji, U. Galler, T. Glaser, Henkel, et al. "Characterization of Different Substrates for Raman Spectroscopic Imaging of Eukaryotic Cells". J. Raman Spectrosc. 2016. 47(7): 773–786.
21. K. Partridge, X. Yang, N.M. Clarke, Y. Okubo, et al. "Adenoviral BMP-2 Gene Transfer in Mesenchymal Stem Cells: In Vitro And In Vivo Bone Formation on Biodegradable Polymer Scaffolds". Biochem. Biophys. Res. Commun. 2002. 292(1): 144–152.
22. L. Zhang, Y.W. Chun, T.J. Webster. "Decreased Lung Carcinoma Cell Density on Select Polymer Nanometer Surface Features for Lung Replacement Therapies". Int. J. Nanomed. 2010. 5: 269–275.
23. F. Sinjab, K. Kong, G. Gibson, S. Varma, et al. "Tissue Diagnosis Using Power-Sharing Multifocal Raman Micro-Spectroscopy and Auto-Fluorescence Imaging". Biomed. Opt. Express. 2016. 7(8): 2993–3006.
24. C.A. Lieber, A. Mahadevan-Jansen. "Automated Method for Subtraction of Fluorescence from Biological Raman Spectra". Appl. Spectrosc. 2003. 57(11): 1363–1367.
25. B.D. Beier, A.J. Berger. "Method for Automated Background Subtraction from Raman Spectra Containing Known Contaminants". Analyst. 2009. 134(6): 1198–1202.
26. N.J. Everall. "Modeling and Measuring the Effect of Refraction on the Depth Resolution of Confocal Raman Microscopy". Appl. Spectrosc. 2000. 54(6): 773–782.
27. N.J. Everall. "Confocal Raman Microscopy: Why the Depth Resolution and Spatial Accuracy Can Be Much Worse Than You Think". Appl. Spectrosc. 2000. 54(10): 1515–1520.
28. K.E. Gascoigne, S.E. Taylor. "How Do Anti-Mitotic Drugs Kill Cancer Cells?" J. Cell Sci. 2009. 122: 2579–2585.